



# Facile processing for instant production of clinically-approvable nanoagents for combination cancer therapy



Milan Gautam<sup>a</sup>, Bijay Kumar Poudel<sup>a</sup>, Zar Chi Soe<sup>a</sup>, Kishwor Poudel<sup>a</sup>, Srijan Maharjan<sup>a</sup>, Sae Kwang Ku<sup>b</sup>, Chul Soon Yong<sup>a</sup>, Sang Woo Joo<sup>c,\*</sup>, Jong Oh Kim<sup>a,\*</sup>, Jeong Hoon Byeon<sup>c,\*</sup>

<sup>a</sup> College of Pharmacy, Yeungnam University, Gyeongsan 38541, Republic of Korea

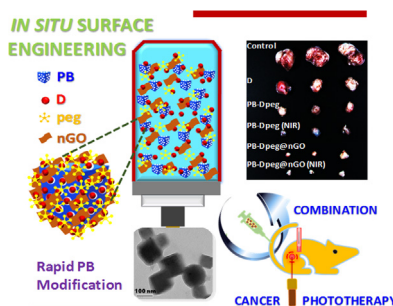
<sup>b</sup> College of Korean Medicine, Daegu Haany University, Gyeongsan 38610, Republic of Korea

<sup>c</sup> School of Mechanical Engineering, Yeungnam University, Gyeongsan 38541, Republic of Korea

## HIGHLIGHTS

- Prussian blue (PB) was selected as both a drug vehicle and a light-activatable agent.
- Porous PB was mixed with anticancer drug and stealth compound using a vibrating nozzle.
- The *in situ* engineered PB nanoagents produced comparable combination cancer therapies.

## GRAPHICAL ABSTRACT



## ARTICLE INFO

### Keywords:

Combination cancer therapy  
Therapeutic nanoagent  
Clinically-approvable  
Prussian blue nanocage  
Vibrating nozzle spraying

## ABSTRACT

In order to produce more efficacious cancer treatments, combination therapies using stimuli-responsive therapeutic nanoagents (NAs) have been extensively researched over the past two decades. However, unexpected side effects, systemic toxicities, and validation and cost issues of newly developed NAs have hampered their practical application. The use of clinically-approved agents as NAs using particle engineering or modification is receiving renewed attention as an alternative strategy for the development of cancer nanomedicines. However, this approach is limited for postsurgical cancer treatments *via* external application to the surgical site; thus, the development of a realizable strategy to engineer clinically-approved agents for a broad application of cancer nanotherapeutics is still an important challenge. In this study, *in situ* assembly of NAs consisting of clinically-approvable Prussian blue nanocages (PB NCs), doxorubicin (D), an anticancer drug, and polyethylene glycol (peg), a stealth component was implemented *via* vibrating nozzle spraying for the production of a combination cancer phototherapy. The porous structure of PB NCs was ideal for loading D and peg, forming PB-Dpeg NAs to produce combination phototherapeutics, and this property was also useful for spontaneously patching up their surfaces with lateral nanodimensional graphene oxide flakes during assembly, for strengthening photothermal, sustained D release, and stealth effects without significant changes in the size and shape of PB-Dpeg.

\* Corresponding authors.

E-mail addresses: [swjoo@yu.ac.kr](mailto:swjoo@yu.ac.kr) (S. Woo Joo), [jongohkim@yu.ac.kr](mailto:jongohkim@yu.ac.kr) (J. Oh Kim), [postjb@yu.ac.kr](mailto:postjb@yu.ac.kr) (J. Hoon Byeon).

<https://doi.org/10.1016/j.cej.2019.123177>

Received 30 July 2019; Received in revised form 9 October 2019; Accepted 14 October 2019

Available online 15 October 2019

1385-8947/ © 2019 Elsevier B.V. All rights reserved.

## 1. Introduction

To ameliorate the serious side effects and unsatisfactory efficacy of conventional cancer monotherapies, the development of nanoscale multifunctional materials has attracted considerable attention, and is a major focus of nanomedicine [1]. Numerous types of nanoagents (NAs) with stimuli-activatable functions have been investigated over the past two decades with the aim of achieving modulatable drug release with other therapeutic effects, such as photo-, radio-, sono-, and immunotherapeutics, in order to derive combined or synergistic cancer treatments with enhanced permeability and retention (EPR) effects [2,3]. In particular, combination phototherapies based on photo-induced temperature elevation of NAs have been frequently used because of their simplicity, minimal invasiveness, and ability to simultaneously apply chemo- and photothermal therapies under light irradiation [4,5]. Adding stealth (preventing the opsonin interaction and subsequent phagocyte clearance for the extension of circulation time in the bloodstream) components or tumor-targeting molecules to the NAs further enhanced their efficacies by improving selectivity [2]. However, clinical translation of NAs is still limited because of issues in toxicity, side effects, validation and cost. NAs have considerable potential for contracting the shortcomings of conventional therapies and offering new modalities for highly efficacious cancer treatments [4,6,7]. This potential has attracted attention to the possibilities of utilizing clinically-approved agents as nanomedicines via appropriate engineering, to produce therapeutic nanostructures. This approach could increase the predictability of toxicity and side effects, and also offer a rational way to minimize validation and cost issues [8,9].

For these reasons, clinically-approved nanoscale Prussian blue (PB), which has excellent biocompatibility [10,11], is receiving attention as a base material for NA for combinatorial cancer phototherapies due to its near-infrared (NIR) photothermal conversion properties, which originate from charge transfer between  $\text{Fe}^{2+}$  and  $\text{Fe}^{3+}$  ions, and are comparable to that of other inorganic photoresponsive nanomaterials [12–14]. PB nanoparticles (NPs) can be scalably produced by a simple hydrothermal reaction between  $\text{Fe}^{3+}$  and  $[\text{Fe}(\text{CN})_6]^{4-}$  ions under acidic conditions using a one-pot synthesis scheme at very low cost [15–18]. Because they contain small micropores, however, the direct use of pristine PB NPs may restrict their ability to load anticancer drugs and other biofunctional targeting or protecting molecules to achieve desirable therapeutic effects [19,20]. The pristine PB NPs also are physiologically unstable for *in vivo* applications [21]; thus, further particle engineering and/or surface modifications are required to take advantage of PB NPs [7,9]. Recently, the preparation of hollow or porous PB NPs by particle engineering has been researched as a mechanism for generating sufficient space for carrying anticancer drugs and other guest molecules for NIR- or pH-triggered combination cancer therapies [22–26]. Chemical or biological surface modifications have also been done to achieve modulatable drug release, tumor accumulation, and stealth effects in PB NPs [27–31]. However, these modifications usually involve multiple reactions based on a range of ingredients, involving separations and purifications which might induce unpredictable interference between the components [21]. It is therefore desirable to develop simpler and more realizable strategies for engineering PB NPs, incorporating molecules that facilitate the practical application of clinically-approved multifunctional NAs for effective cancer treatments.

The development of sprayable solutions containing therapeutic agents to form anticancer NAs is receiving renewed attention in nanomedicine as a convenient way to utilize clinically-approved ingredients [3,4,32]. The spraying technique is able to simply and rapidly produce all-in-one droplets by mixing solutions containing the necessary components [33], and can be modulated to control the size, shape, and structure of the resulting materials by applying an electric field to the spray nozzles [34]. The preparation of optimal solutions has recently been attempted in order to scalably fabricate devices for other emerging

technologies, such as solar cells and electrochemical systems [35,36]. However, the use of the spraying technique is limited to the external application of NAs for postsurgical cancer treatments [3,4,32], although sprayed NAs have also been used recently for diagnostic and phototherapeutic purposes [37,38]. In order to achieve a broad cancer therapeutic application, the development of an optimal composition of the sprayable solution and a compatible spraying system is required for the timely engineering of clinically-approved components for more clinically relevant administration routes.

To this end, we designed and prepared a clinically-approved agent containing PB, which was engineered *in situ* with the inclusion of an anticancer drug and a stealth component to produce particulate NAs using a vibrating nozzle spray. The NAs were constructed as composites of PB nanocage (NC), doxorubicin (D), an anticancer drug, and polyethylene glycol (peg), a stealth component, and is called PB-Dpeg. The peg was selected because of its clinical availability. It can improve the biocompatibility and colloidal stability of NAs under physiological conditions, and also produce longer systemic circulation, increasing its levels of accumulation in tumors [23,39]. In order to generate porous structure in the PB, it was synthesized using a one-pot hydrothermal reaction to induce nucleation and the growth process by adding potassium ferricyanide,  $\text{K}_3\text{Fe}(\text{CN})_6$ , into an acidic solution containing polyvinylpyrrolidone (PVP), as shown in Fig. S1A [40]. By simply prolonging the reaction time at a constant bath temperature of 85 °C, the porosity of cubical PB NPs from a 10-h reaction was achieved to be that of PB NCs from a 30-h reaction through the partial decomposition and reduction of  $\text{K}_3\text{Fe}(\text{CN})_6$  under acidic conditions in the presence of PVP. The separated PB NCs were dispersed in buffered saline, and this dispersion was mixed with a solution of D and peg before spraying. The mixture solution containing all of the components was injected onto a thin plate consisting of nozzles with an approximately 4  $\mu\text{m}$  hole diameter, with electromechanical vibration of 128 kHz, as shown in Fig. S1B. From the nozzles, the solution was extruded as all-in-one droplets, and fell directly into buffered saline through ambient drying to form particulate PB-Dpeg before dispersal in the saline. The porosity of the PB NCs was appropriate for the loading of D and peg molecules onto the surfaces during drying, *via* adsorption. The PB-Dpeg dispersion was then assessed for anticancer efficacy in the absence and presence of NIR irradiation in *in vitro* and *in vivo* models (Fig. 1). To further enhance the efficacy of the combination therapy, lateral nanodimensional graphene oxide (nGO, 80–100 nm) flakes prepared using a green process [41] were added into the mixture solution for the spray, to patch up the surfaces of the PB-Dpeg with tight adherence because of capillary action. nGO was selected as the enhancer because of its functionality, flexibility, dispersion stability, and low toxicity [42–45], as well as to conform to the “more is better” paradigm to improve the efficacy and survival of photothermal cancer therapy [46]. The resulting PB-Dpeg@nGO NAs exhibited better photothermal conversion and stability, sustained D release, and tumor accumulation in comparison with the PB-Dpeg in the combination phototherapy, without significant changes in the original size and shape of the PB-Dpeg.

## 2. Materials and methods

### 2.1. Preparation PB NCs and *in situ* engineering with D, peg, and nGO

PB NCs to be engineered with D, peg, and nGO were first prepared by dissolving 792 mg of  $\text{K}_3[\text{Fe}(\text{CN})_6]$  (Sigma-Aldrich, USA) and 4.5 g of PVP (Sigma-Aldrich, USA) in 0.001 M HCl (50 mL; Sigma-Aldrich, USA) solution. After 30 min stirring at room temperature, the yellowish solution was obtained, and this solution was then subjected to an electrically heated chamber for further reaction (Fig. S1) to obtain bluish dispersion at 85 °C for 24 h. To examine the formation of NC structure, bluish particles in the dispersion were collected by centrifugation after 30 h reaction, and the particles were washed thrice with distilled water and subsequently dried for TEM observation. The particles from

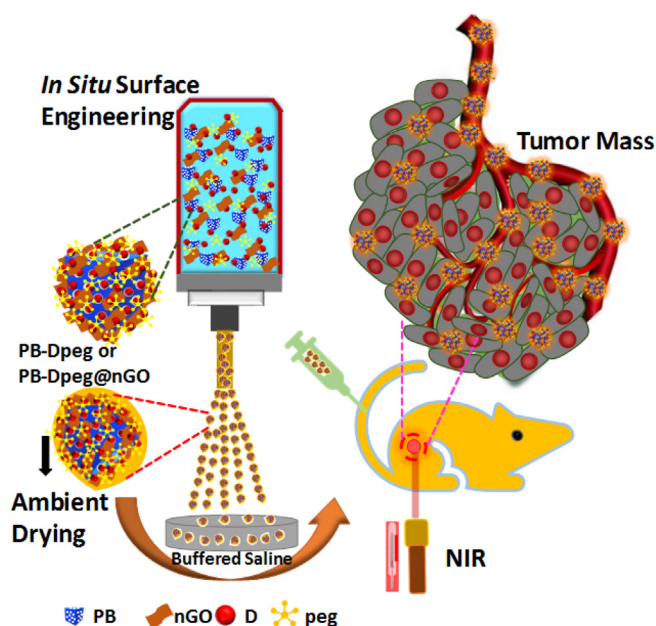


**Fig. 1.** Schematic of *in situ* surface engineering of PB NCs with D, peg, and nGO for combination cancer phototherapy. The PB NCs were mixed with a solution of D and peg in the absence and presence of nGO and loaded into a vibrating nozzle spray device. The solution was sprayed as all-in-one droplets for free-fall into buffered saline and subjected to ambient drying to form particulate PB-Dpeg or PB-Dpeg@nGO NAs. The NA dispersed saline was intravenously injected into mice to assess its antitumor efficacy in the absence and presence of NIR irradiation.

different reaction times (10 h and 20 h) were also collected, washed, and dried for TEM observation for comparison.

In order to engineer the NCs with clinically-approved compounds, the prepared NCs were dispersed in PBS, and the dispersion was added into a mixture solution of D (at different % w/w) and peg (1 mg mL<sup>-1</sup>) to form PB-Dpeg dispersion for vibrating spray. This dispersion was connected to the reservoir of a vibrating nozzle device (operating frequency, 128 kHz), and freely fallen down from the nozzle as all-in-one droplets into PBS solution for *in vitro* and *in vivo* experiments. The mean diameter of the droplets before drying was  $2.7 \pm 0.2 \mu\text{m}$ , which was measured using optical particle (1.108, Grimm, Germany). The distance between the nozzle and PBS-filled bottle was selected for complete solvent extraction (*i.e.*, solidification into PB-Dpeg NAs) from the droplets during free-fall. In order to patch-up the NC surface during free-fall, nGO flakes [47] were added (1-NC:1-nGO ratio) to the NCs dispersion containing D and peg, resulting in the formation of PB-Dpeg@nGO NAs. The *in situ* PB engineering was performed inside a clean bench to prevent particle contamination.

## 2.2. Characterization of PB-Dpeg and PB-Dpeg@nGO NAs

The size distributions and zeta potentials of PB-Dpeg and PB-Dpeg@nGO NAs, including PB NCs were analyzed using a DLS system (NanoS90, Malvern Instruments, UK). The light absorption characteristics of the samples were analyzed using a UV-visible spectrophotometer (U-2800, Hitachi, Japan). The morphologies of the samples were observed using a TEM (H7600, Hitachi, Japan) at an accelerating voltage of 100 kV, while low- and high-magnification TEM images of nGO flakes were obtained using another TEM (Tecnai G<sup>2</sup> F20 S-TWIN, FEI, USA). The adsorption isotherm and pore size distribution of PB NCs were obtained using a porosimeter (ASAP 2010, Micromeritics, USA). The surface chemistry, crystalline property, and thermal behavior and weight loss of PB-Dpeg, PB-Dpeg@nGO, and individual components were analyzed via a FTIR spectrometry (Nicolet Nexus 670, Thermo

Fisher Scientific, USA), X-ray diffractometry (Malvern Pananalytical, UK), and DSC (Q200, TA Instruments, USA) and thermogravimetric (SDT-Q600, TA Instruments, USA) analysis, respectively. In order to examine NIR-induced photothermal conversion activity, PB-Dpeg and PB-Dpeg@nGO NAs were dispersed in PBS as chosen concentrations (10, 20, 30, 40, and 50  $\mu\text{g mL}^{-1}$ ). NIR irradiation (808 nm, 2 W cm<sup>-2</sup>) was applied onto the dispersions, while temperatures of the dispersions were digitally monitored using a thermal camera (Therm-App TH, Israel) during the irradiation.

## 2.3. EE and LC

The EE of D in PB-Dpeg and PB-Dpeg@nGO NAs was evaluated using a centrifugal ultrafiltration device (Amicon®, MWCO 10000 Da, Millipore, USA) at 5000 rpm (for 10 min). The D concentration was determined at a wavelength of 485 nm using the UV-visible spectrophotometer. The percent EE and LC of D were estimated using the following formula:

$$EE(\%) = C_{ED}/C_{TD} \times 100(\%)$$

$$LC(\%) = C_{TD} - C_{UD}/C_{TS} \times 100(\%)$$

where,  $C_{ED}$ ,  $C_{TD}$ ,  $C_{UD}$ , and  $C_{TS}$  are the concentrations of the D entrapped within the samples, total D, unbound D, and total samples, respectively.

## 2.4. In vitro D release

The *in vitro* release profile of D from PB-Dpeg and PB-Dpeg@nGO NAs were measured via a dialysis method. 1 mL of each NA was placed in a dialysis tubing (Spectra/Por, MWCO 3500 Da, Spectrum Labs, USA) and successively immersed in 25 mL of release medium PBS (pH 7.4) or acetate buffered saline (pH 5.0). The samples were maintained at 37 °C and 100 rpm, and the aliquots of samples (0.5 mL) were then withdrawn at predetermined time intervals and followed by replenishment with an equal amount of fresh release media. The released amount of D was determined using the UV-visible spectrometer at a wavelength of 485 nm.

## 2.5. Cell viability

The *in vitro* viability of PANC-1 cells (Korean Cell Line Bank, Korea) was assessed after 24 h or 48 h incubation with NAs using MTT assay (Sigma-Aldrich, USA). Cells were first seeded into a 96-well plate ( $1 \times 10^4$  cells per well) and treated with NAs, including individual components for comparison in the absence and presence of NIR irradiation. Following the incubation, the MTT solution was added into each well, and absorbance of formazan crystals dissolved in dimethyl sulfoxide (Sigma-Aldrich, USA) was obtained using a microplate reader (Multiskan EX, Thermo Scientific, USA) at a wavelength of 570 nm.

## 2.6. Cellular internalization and uptake

**Confocal microscopy:** The internalization of PB-peg and PB-peg@nGO into cells was investigated using a CLSM (K1-Fluo, Nanoscope Systems, Korea). Cells were seeded on a coverslip placed on a 12-well plate ( $2 \times 10^4$  cells per well) and incubated overnight at 37 °C in 5% CO<sub>2</sub> environment. The cells were treated with samples (1, 3, and 5  $\mu\text{g mL}^{-1}$ ) for different intervals. LysoTracker green (100 ng mL<sup>-1</sup>; Thermo Fisher Scientific, USA) was used to trace the lysosome within the cells. The treated cells were washed with PBS, fixed in 4% formaldehyde, and finally mounted on a glass slide for observation using the CLSM.

**FACS analysis:** To analyze the cellular uptake of PB-Dpeg and PB-Dpeg@nGO NAs, cells were seeded at a density of  $1 \times 10^5$  cells per well in a 6-well plate, and successive treatments were similarly followed the procedures for the CLSM observation. The treated cells were washed

with cold PBS, trypsinized, and washed to form a cell pellet. This was redispersed in PBS (1 mL) for flow cytometry analysis (FACSCalibur™, BD Bioscience, USA).

## 2.7. In vitro apoptosis assay

**Live/dead assay:** 750  $\mu\text{M}$  of PI and 6.7  $\mu\text{M}$  of acridine orange (AO) solutions were used to stain the PB-Dpeg- and PB-Dpeg@nGO-treated cells ( $1 \times 10^5$  cells per well) in the absence and presence of NIR irradiation. PI-positive cells represent dead cells, while AO-positive cells represent live cells.

**FACS analysis:** After 48 h treatment similar procedures with the live/dead assay, treated cells were harvested, mixed with binding buffer, and stained with PE-Annexin V and 7-AAD for 15 min. The cells were diluted with binding buffer and finally analyzed using the flow cytometry analysis.

**Hoechst fluorescent staining:** Hoechst 33,342 staining was performed to confirm the apoptosis induction from treatment with PB-Dpeg and PB-Dpeg@nGO NAs. Cells were seeded ( $1 \times 10^5$  cells per well) in 12-well plates for 24 h for adhesion. After 48 h of treatment, treated cells were washed twice with PBS, stained with the 33,342 ( $10 \mu\text{g mL}^{-1}$ ), and examined using a fluorescence microscope (Eclipse Ti, Nikon, Japan).

## 2.8. In vitro ROS measurement

The production of intracellular ROS was measured using the fluorescence microscopy with oxidative condition sensitive fluorescent dye (DCFH-DA). Cells were first treated with PB-Dpeg and PB-Dpeg@nGO NAs for 48 h, washed with PBS, and incubated in a culture medium containing  $30 \mu\text{mol L}^{-1}$  of DCFH-DA for 30 min in the dark. The cells were then washed with PBS, and the ROS was observed using the fluorescent microscope.

## 2.9. Cell migration assay

Cells were seeded in 12-well plates and grown for confluence. Two parallel lines running across each well were scratched on the underside of the plate and treated with PB-Dpeg and PB-Dpeg@nGO NAs. To examine cell migration, images were captured using an inverted microscope (CKX41SF, Olympus, Japan) with iSolution Lite digital imaging system at 24 h or 48 h postscratch.

## 2.10. Hemolytic toxicity

The hemocompatibility of NAs, including individual components was assessed using Sprague Dawley rat blood. The sampled blood was placed in a heparinized tube and centrifuged (3500 rpm, 10 min) to separate red blood cells from the blood. 1 mL of diluted (saline solution) blood was injected into each test tube containing 10 mL of saline, treated with each sample (equivalent to  $5 \mu\text{g mL}^{-1}$  D), and gently mixed and incubated at  $37^\circ\text{C}$  for 30 min. The positive and negative controls were prepared as 1 mL of diluted blood with 9 mL of water and 1 mL of diluted blood with 9 mL of saline, respectively. After incubation, all the samples were centrifuged at 3500 rpm for 10 min, and the supernatants were optically analyzed using the UV–visible spectrometer at 540 nm. The percent hemolysis was estimated using the following equation:

$$\text{Hemolysis}(\%) = (A_s - A_{s0}/A_{s100} - A_{s0}) \times 100(\%)$$

where,  $A_s$ ,  $A_{s0}$ , and  $A_{s100}$  are the absorbances of sample, negative control, and positive control, respectively.

## 2.11. In vivo biodistribution and photothermal imaging

PANC-1 tumor xenograft was developed in 5 weeks Balb/c nude

mice by injecting  $1 \times 10^7$  cells suspended in 200  $\mu\text{L}$  of serum-free fresh media into the right flank of mice via subcutaneous injection. The tumor-bearing mice were intravenously injected with Cy5.5-labeled PB-peg and PB-peg@nGO via the tail vein. At predetermined time intervals (0.5, 6, 12, 24, and 48 h postinjection), the fluorescent images of mice were obtained using a NIR fluorescence imaging system (FOBI, NeoScience Korea). Furthermore, the mice were sacrificed after 48 h postinjections, and tumors and major organs (heart, spleen, kidney, lung, and liver) were collected, washed, and imaged to confirm the distribution. To examine photothermal activity of NAs in *in vivo* level, NIR irradiation ( $808 \text{ nm}$ ,  $2 \text{ W cm}^{-2}$ ) was applied onto the tumor area for 5 min after 24 h postinjection. Temperature contours of the treated mice were recorded using the thermal camera during the irradiation.

## 2.12. In vivo antitumor study

Five-week-old Balb/c nude mice were used to evaluate antitumor efficacy of NAs. After the tumor size reached  $\sim 100 \text{ mm}^3$ , the mice were randomly divided into six groups. The all mice were intravenously injected via the tail vein at the same dose ( $10 \text{ mg D kg}^{-1}$ , once every four days, four times), while the control groups were treated with saline instead. NIR irradiation ( $808 \text{ nm}$ , 2 min,  $2 \text{ W cm}^{-2}$  for rapid *in vivo* temperature elevation [ $\sim 50^\circ\text{C}$ ] within 2 min to suppress side effects) was applied onto the tumor area 24 h postinjection, and changes in tumor volume and body weight were monitored for 24 days. The care and use of the mice were performed according to the Guidelines for Care and Use of Laboratory Animals of Yeungnam University and approved by the Animal Ethics Committee of Yeungnam University.

## 2.13. Histopathological analysis

In order to assess the histopathological and histomorphometrical changes, representative tumor masses from the xenograft mouse model were removed, and changes in tumor masses were observed using H&E staining. The immunoreactivity changes in tumor masses against the apoptotic markers (cleaved caspase-3 and cleaved PARP), angiogenesis marker (CD31), and tumor cell proliferation marker (Ki-67) were also analyzed and estimated after treatments with different samples.

## 2.14. Statistical analysis

The significance between the groups was evaluated using one-way ANOVA via Fisher's LSD test and Student's unpaired *t*-test.

## 3. Results and discussion

Fig. 2A shows low- and high-magnification TEM images of PB NPs at different times during the hydrothermal reaction (Fig. S1). The 10-h reaction produced cubical structures of approximately 50 nm lateral dimension, and the size of the particles increased with increasing reaction time due to autonucleation and the subsequent growth of PB crystals on the preformed surfaces, which matched the sizes obtained by dynamic light scattering (DLS) measurements (Fig. S2). After a 30-h reaction, the polydispersity index (PDI) was significantly reduced, possibly due to the partial decomposition of  $\text{K}_3\text{Fe}(\text{CN})_6$  removing scattering particles in the presence of PVP [48]. This also generated pores on PB NPs to be PB NCs, which when examined using TEM exhibited different gradations from those of the 30-h reaction. A representative high-magnification TEM image of PB NCs exhibited *d*-spacings of 0.50 nm and 0.31 nm, which matched the (2 0 0) and (2 2 0) planes of the PB, respectively [49]. This observation implies that the crystallinity of PB could be maintained over the course of the hydrothermal reaction, although the pores were generated by the partial decomposition. As shown in Fig. 2B, the adsorption isotherm (specific surface area:  $534.3 \text{ m}^2 \text{ g}^{-1}$ ; pore volume:  $0.459 \text{ cm}^3 \text{ g}^{-1}$ ) and pore size distribution (inset, 4.9 nm average pore diameter) obtained using a



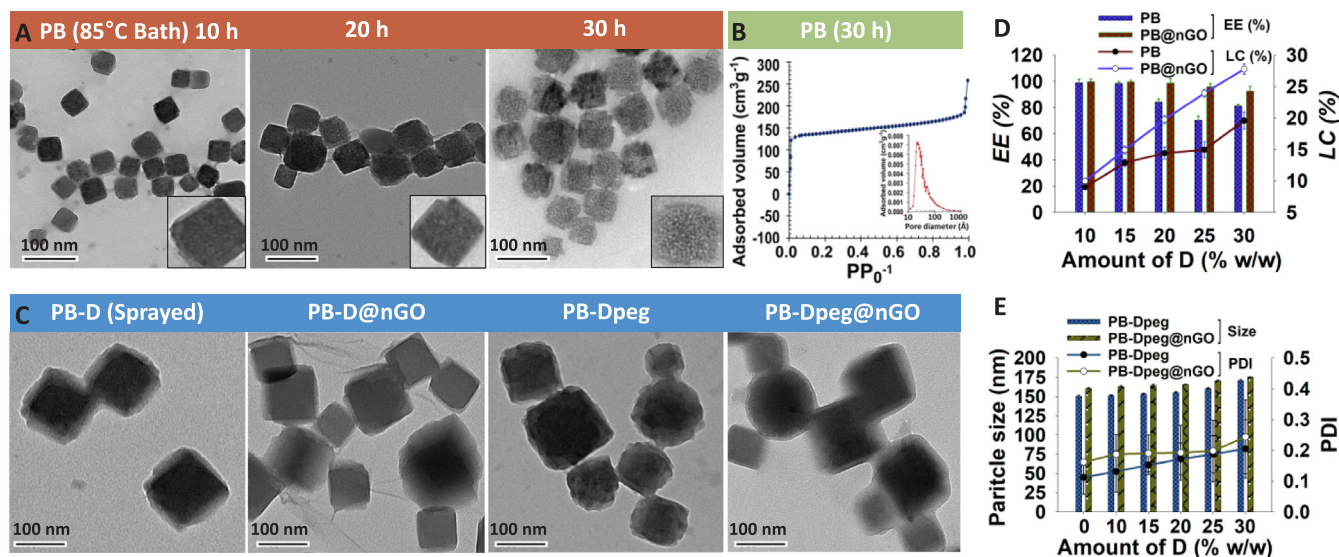


**Fig. 2.** Morphological, textural, D loading, and DLS properties of PB-Dpeg and PB-Dpeg@nGO NAs, including individual components. (A) Low- and high-magnification TEM images of PB structures with different hydrothermal reaction times. (B) Adsorption isotherm and pore size distribution of PB during a 30-h hydrothermal reaction. (C) Representative TEM images of PB-D and PB-Dpeg in the absence and presence of nGO. The PB NCs are the particles resulting from a 30-h hydrothermal reaction. (D) EE and LC of PB NC in the absence and presence of nGO. (E) Hydrodynamic particle size and PDI of PB-Dpeg in the absence and presence of nGO.

porosimeter represented the mesoporous property of the NCs. The gradation of PB NCs co-sprayed with D or Dpeg molecules was changed again as dark (Fig. 2C), proving that the mesopores generated are capable of loading D or Dpeg molecules via adsorption. Co-spraying with nGO, whether PB-D@nGO or PB-Dpeg@nGO, only shows blurs on the particles without notable changes in shape in the TEM observations, indicating that PB-D or PB-Dpeg is tightly patched up with nGO flakes, probably due to capillary suction, in comparison to the crumpled shape of nGO from spraying (Fig. S3A). The tight adherence was further supported by zeta potential measurements (Fig. S3B), in which there were no significant differences in surface charge between the nGO-patched samples. This enhanced the encapsulation efficiency (EE) and loading capacity (LC) of PB NCs by increasing the D content (10–30% w/w) in the spraying solution (Fig. 2D), even with peg (Fig. S3C), a finding which implies that patching up the NC with nGO is effective to facilitate tight loading of D. This loading produced clearer responses in zeta potential for the nGO-inclusive configuration compared with those for the NC-only by increasing the D content (Fig. S3D). Furthermore, no significant increases in DLS size and PDI were observed in PB-Dpeg@nGO for different D contents compared with PB-Dpeg (Fig. 2E). EPR-enabling sizes (< 200 nm) were achieved for both PB-Dpeg and PB-Dpeg@nGO NAs, suggesting that the engineering approach we developed is suitable for the assembly of NAs *in situ* without complex reactions, using pre- and post-treatments. In addition, EE and LC, as well as hydrodynamic size distribution and zeta potential of the NAs from co-spraying were compared with those from hydrothermal reaction, as noted in Table S1. The NAs from co-spraying exhibited comparable or better properties, implying that hydrothermal reaction with pre- and post-treatments can be minimized by using this spraying strategy.

In order to examine the light-activatable properties of the PB NCs, UV–visible absorption spectra were obtained for particle concentrations ranging from 10 to 50  $\mu\text{g mL}^{-1}$  using a UV–visible spectrophotometer (Fig. S3E). The NC dispersions exhibited distinct absorptions for the wavelength range between 500 nm and 1000 nm, indicating their relevance to NIR susceptibility. NIR (808 nm, 2 W  $\text{cm}^{-2}$ ) were irradiated onto PB-Dpeg (Fig. 3A) or PB-Dpeg@nGO (Fig. 3B) dispersions (10–50  $\mu\text{g mL}^{-1}$ ) for five minutes, and the temperature contours recorded using a thermal camera. Significant temperature elevations were observed for PB-Dpeg (Fig. S3F), and these were further intensified for PB-Dpeg@nGO due to the  $\pi$ -network of nGO (Fig. S3G). The physical

robustness of nGO and thermal storage from nGO adherence on PB NC exhibited better stability of photothermal activity after five cycles compared with PB-Dpeg (Fig. S3H), suggesting that adding nGO could enhance both tight D loading and the stable photothermal conversion of PB NCs. The loading of D and further addition of nGO onto PB NCs were determined using UV–visible (Fig. S4A) and Fourier-transform infrared (FTIR, Figs. 3C and S4B) spectroscopy. Absorption peaks at around 480 nm for PB-Dpeg and PB-Dpeg@nGO verified D loading, while transmittance bands at around 1720  $\text{cm}^{-1}$  confirmed the loading onto the two NAs [50]. Transmittance bands at around 2070  $\text{cm}^{-1}$  matched the stretching of  $\text{Fe}^{2+}\text{--CN--Fe}^{3+}$  in the two NAs (core PB NCs) [14], and bands at around 3420  $\text{cm}^{-1}$  corresponded to the terminal hydroxyl groups in peg [51]. Bands at around 1050  $\text{cm}^{-1}$ , 1390  $\text{cm}^{-1}$ , and 1610  $\text{cm}^{-1}$  were attributed to stretching vibrations of C–O, O–H, and C=O on the nGO surface, respectively [52], supporting the patching up of PB-Dpeg with nGO. The thermogram of D from differential scanning calorimetry (DSC), at 10  $^{\circ}\text{C min}^{-1}$  heating rate exhibited the glass transition temperature of 205.4  $^{\circ}\text{C}$ , which was reduced by 187.7  $^{\circ}\text{C}$  for PB-Dpeg, as shown in Fig. 3D. The peak intensity representing thermal deformation of D for PB-Dpeg@nGO was significantly reduced compared with that of PB-Dpeg, suggesting that nGO adhered to the PB-Dpeg ensures the stability of D in the NA. The tight adherence of nGO was further examined using X-ray diffractometry (XRD), and the characteristic bands of D were observed to have nearly disappeared in the two NAs (Fig. 3E), demonstrating successful D loading inside PB NCs. Only the characteristic bands for PB could be clearly observed at 17.6 $^{\circ}$ , 24.6 $^{\circ}$ , 35.3 $^{\circ}$ , and 39.4 $^{\circ}$  for PB-Dpeg, corresponding to the (2 0 0), (2 2 0), (4 2 0), and (4 0 0) planes of the face-centered cubic PB lattices, respectively (Fig. S4C) [14]. The intensity of the bands was reduced by adding nGO, and a band at 9.4 $^{\circ}$  was also observed, matching the (0 0 1) base plane of nGO [53]. A small band between the first two peaks for PB, attributable to the major peak of peg, suggested the existence of the stealth component on the surface of the PB-Dpeg@nGO [54]. In addition, thermogravimetric analysis was performed to examine content of peg and nGO in the NAs, as shown in Fig. 3F, where PB-Dpeg exhibited about 4.4% in weight loss as that of PB-D, representing peg content in the NAs; thus, the weight loss of nGO was determined as 5.3%. The physicochemical characterization of the two NAs suggested the presence of properties which collectively demonstrate chemotherapeutic and stealth effects with photothermal activity for combination cancer

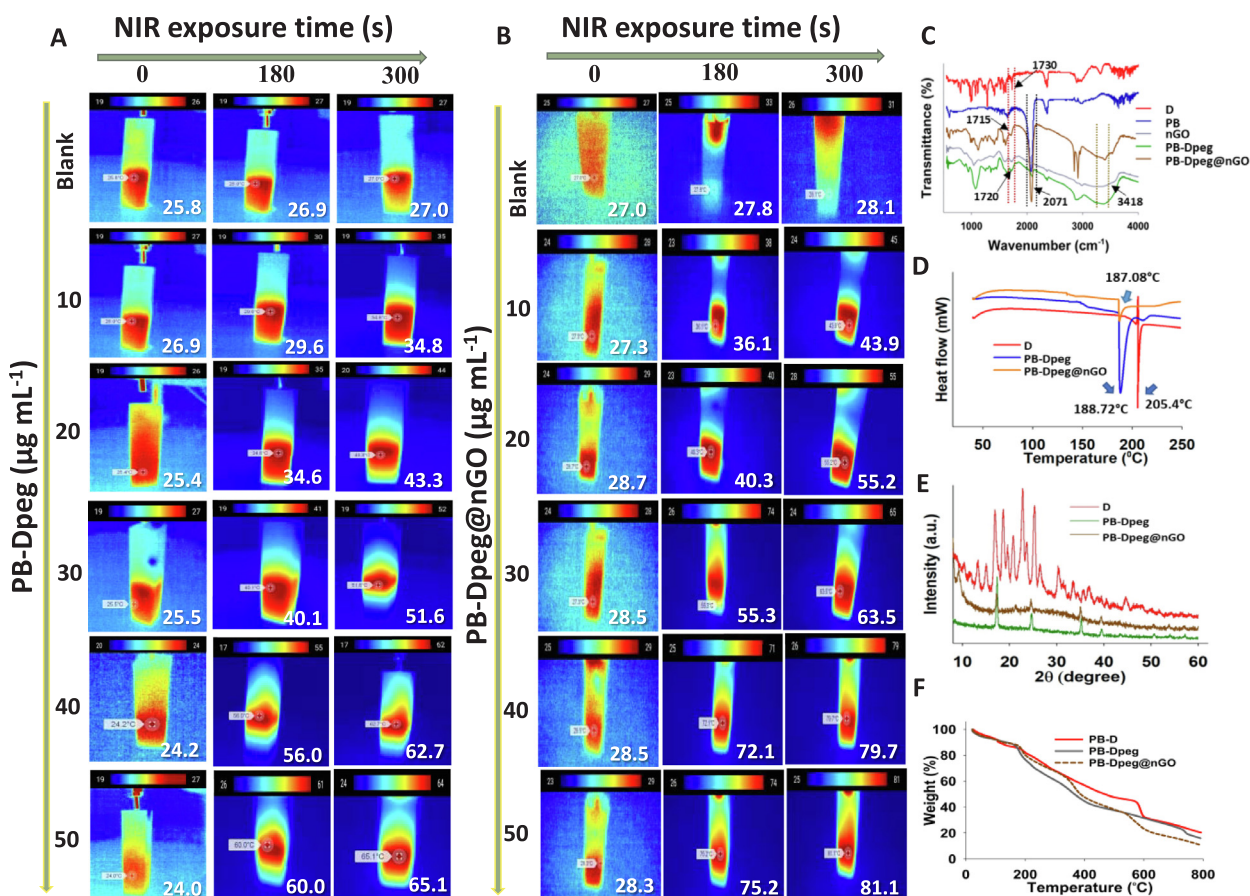


**Fig. 3.** Physicochemical properties of NAs from in situ engineering of PB NCs. (A, B) Temperature contours obtained using a thermal camera from time- and concentration-dependent photothermal conversion activity of PB-Dpeg dispersion in the absence and presence of nGO under NIR irradiation at 808 nm and 2 W cm<sup>-2</sup>. (C) FTIR spectra of PB-Dpeg and PB-Dpeg@nGO NAs, including individual components for comparison. (D, E) DSC thermograms and XRD profiles of PB-Dpeg and PB-Dpeg@nGO NAs, including individual D for comparison. (F) Thermogravimetric curves of PB-Dpeg and PB-Dpeg@nGO NAs, including PB-D for analyzing weight losses of peg and nGO.

treatment from the *in situ* engineering of clinically-approvable components.

In order to assess the *in vitro* efficacy of PB-Dpeg and PB-Dpeg@nGO NAs, cumulative D release profiles were obtained at 72 h at pH 7.4 (normal physiological condition), 6.5 (tumor cell environment), and 5.0 (acidic cellular endosomes), as shown in Figs. 4A and S4D (the enlarged one for the first 12 h). The cumulative D release from PB-Dpeg NAs was ~43% under physiological conditions of pH 7.4, and was significantly increased, by around 56% at pH 6.5 and 71% at pH 5.0, under acidic conditions, a simulated tumor microenvironment due to the protonation of amino groups in D, supporting the contention that the NA is workable for pH-responsive D release [55,56]. Sustained release was further enhanced for PB-Dpeg@nGO NAs (~36% at pH 7.4 and ~62% at pH 5.0) because the nGO patched onto PB-Dpeg reduces the off-target effect of chemotherapeutics from the PB-Dpeg architecture. This observation implies that the *in situ* engineering approach developed in this study warrants further investigation for modulatable sustained D release without additional chemical and purification processes. To evaluate the efficacy of this sustained D release with photothermal activity *in vitro*, using a human pancreatic cancer (PANC-1) cell line, a 3-(4,5-dimethylthiazol-2-yl)-2,5-diphenyl tetrazolium bromide (MTT) assay was used to measure the cytotoxicities of the two NAs, including individual components. Fig. S5 shows the viabilities of PANC-1 cells treated with individual components and D-excluded NAs for incubation times of 24 h and 48 h and concentrations of 10–50 μg mL<sup>-1</sup> in the absence and presence of NIR irradiation. All configurations exhibited viabilities greater than 80% in the absence of NIR irradiation, and the

viabilities were decreased by 20–30% after NIR irradiation. These results imply that both the base components and the NAs are biocompatible, but they can suppress cell proliferation by photothermal activity in the presence of NIR irradiation. The configurations containing both PB NC and nGO exhibited greater cytotoxic effects than the individual ones because of enhanced photothermal activity. The inclusion of D into PB-peg@nGO thus significantly enhanced cytotoxic effects in the presence NIR irradiation, even at low D concentrations (< 10 μg mL<sup>-1</sup>), exhibiting combination phototherapeutics (Fig. 4B). The concentration-dependent (Fig. 4C and 4D) and time-dependent (Figs. S6A and S6B) intracellular uptake of D-excluded NAs was observed using confocal laser scanning microscopy (CLSM). As can be seen in the overlay images, the PB-peg@nGO architecture, which contains both PB NC and nGO, showed greater lysosomal uptake compared with PB-peg, supporting the contention that nGO adherence on PB-peg can enhance the stealth effect of PB-peg that may facilitate site-selective D release for effective antitumor effects. The intracellular uptake of D-included NAs was examined using fluorescence-activated cell sorting (FACS) analysis (Figs. S6C and S6D). Even though the two NAs clearly exhibited both concentration- and time-dependent uptake, there were significant differences in uptake between the NAs, further demonstrating the effect of nGO adherence. The anticancer activity was also examined using live and dead assays for cells treated for 48 h with PB-Dpeg and PB-Dpeg@nGO NAs (Fig. 4E), including D-excluded ones (Fig. S7A) and individual components (D and nGO) in the absence and presence of NIR irradiation at 808 nm, 2 W cm<sup>-2</sup> for five minutes. Similar to the results of the MTT assay (Figs. 4B and S5), the inclusion of



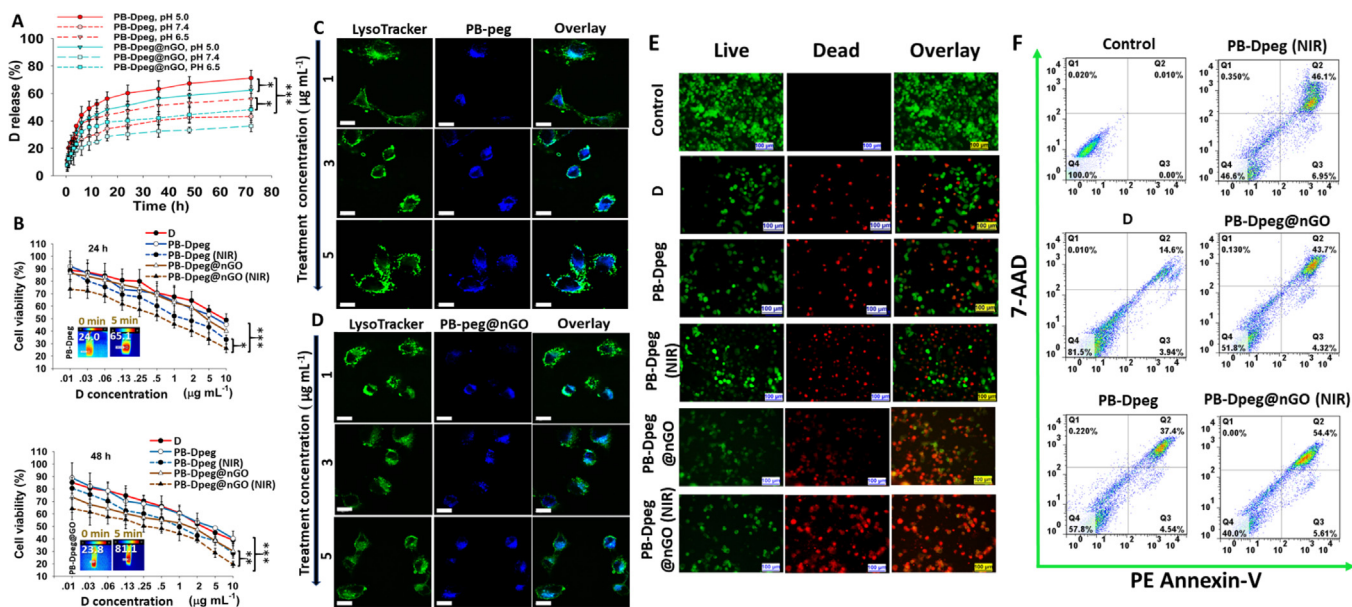


**Fig. 4.** *In vitro* therapeutic activity of NAs on PANC-1 cells in the absence and presence of NIR irradiation at 808 nm and  $2 \text{ W cm}^{-2}$ . (A) D release profiles from PB-Dpeg and PB-Dpeg@nGO NAs at different pH conditions ( $*p < 0.05$  and  $***p < 0.001$ ). (B) D concentration-dependent cytotoxic responses of cells treated with the NAs, including individual D for comparison after 24 and 48 h incubation ( $*p < 0.05$ ,  $**p < 0.01$ , and  $***p < 0.001$ ). Insets show representative temperature contours of the NA dispersions at 0 min and 5 min NIR irradiation. (C) CLSM images of cells treated with D-excluded NAs to avoid fluorescence interference at  $1\text{--}5 \mu\text{g mL}^{-1}$  for 60 min. LysoTracker green was used for tracking lysosomes, while the blue color originated from PB itself (scale bars:  $20 \mu\text{m}$ ). (E, F) Live and dead images (scale bars:  $100 \mu\text{m}$ ) and FACS profiles of cells treated with PB-Dpeg and PB-Dpeg@nGO NAs (five minutes irradiation for “NIR” cases), including individual D for comparison. (For interpretation of the references to color in this figure legend, the reader is referred to the web version of this article.)

D into PB-peg@nGO produced the greatest activity, and this was further confirmed by analyzing the apoptosis profiles of the treated cells using flow cytometry (Figs. 4F and S7B). In a Hoechst staining assay, bright spots, indicated by green arrows, representing the condensed chromatin of cell nuclei could be observed. These spots represent morphological changes in the treated cells because of apoptosis [57]. The highest frequencies of both bright Hoechst stain and dichloro-dihydro-fluorescein diacetate (DCFH-DA) fluorescence (Fig. S7D) for PB-Dpeg@nGO NAs in the presence of NIR irradiation could thus be associated with the highest production of reactive oxygen species (ROS) from enhanced combination chemo- and phototherapeutic effects. In the cell migration study (Fig. S7E), the phototherapeutic effects of the two NAs under NIR irradiation were also effective in inhibiting cancer cell migration from the NAs to distant regions, as indicated by the dark dots away from the center, implying that NIR irradiation of the NAs may be able to reduce the potential for cancer cells to migrate distant organs, thus suppressing metastasis.

In order to assess the *in vivo* biodistribution of NAs, the cyanine 5.5 (Cy5.5)-labeled D-excluded NAs PB-peg-Cy5.5 and PB-peg@nGO-Cy5.5 were administered to PANC-1 tumor-bearing mice *via* intravenous injection and monitored at 0.5, 6, 12, 24, and 48 h. An accumulation of PB-peg@nGO-Cy5.5 was clearly observable 6 h after injection, and was significantly greater than that seen in PB-peg-Cy5.5 (Fig. 5A). The time profiles of fluorescence intensity (Fig. S8A) for the two Cy5.5-labeled NAs were different, demonstrating the critical role of nGO adherence in enhancement of the stealth effect, even *in vivo*. The fluorescence intensities of excised major organs and tumors were measured after sacrificing the mice 48 h postinjection to confirm the tumor-homing capabilities of the two NAs (Figs. 5B and S8B). Even though PB-peg-Cy5.5 NAs accumulated to some extent at the tumor site, considerably more NAs accumulated in the heart and liver, compared with the levels of the PB-peg@nGO-Cy5.5 NAs, an observation which further suggested the effectiveness of nGO incorporation. The greater accumulation of PB-peg@nGO-Cy5.5 NAs in tumors also suggested that their removal *via* the reticuloendothelial system may be delayed, so suitable modification of the dispersion composition of the vibrating spray may modulate

tumor accumulation activity to create better conditions for cancer treatments. *In vivo* temperature elevations of PB-Dpeg and PB-Dpeg@nGO NAs under NIR irradiation of 808 nm,  $2 \text{ W cm}^{-2}$  for five minutes were obtained using a thermal camera, for the evaluation of their tumor cell ablative capabilities (Fig. 5C). The PB-Dpeg and PB-Dpeg@nGO injected groups induced a temperature increase of  $46.8^\circ\text{C}$  and  $57.8^\circ\text{C}$  respectively at the tumor site, whereas the phosphate buffered saline (PBS) treated group exhibited no significant increase (Fig. S8C). The higher photothermal activity of the PB-Dpeg@nGO NAs may be produced by additional heat generation and storage due to nGO adherence on the PB-Dpeg, as well as greater accumulation in tumors due to the enhanced stealth effect. These effects induced the “more is better” configuration to more effectively ablate tumor cells, demonstrating that only two minutes of NIR exposure is sufficient to generate photothermal therapeutics in *in vivo*; the temperature reached around  $50^\circ\text{C}$ .

Tumor volume (Fig. 5D) and body weight (Fig. 5E) were measured to assess the systemic effects of NA injection in the absence and presence of NIR irradiation. Our investigations included immunohistological (Fig. 5F) and histopathological (Fig. 5G) analyses of tumor mass. Significant increases in tumor volume for the D-treated group were observed during the monitoring period of 24 days, suggesting that treatment with D alone did not cause as much tumor cell destruction as the other treatment configurations (G3–G6). In particular, NIR irradiation greatly suppressed tumor growth *via* the combination chemo- and photothermal therapies, in which NIR induced burst D release at the tumor site and also caused thermal ablation for the destruction of tumors by hyperthermia. When body weight was monitored, individuals exposed to the D treatment showed significant weight loss, which matched the monitored tumor volumes. Other configurations (G3–G6) showed a trend toward increasing body weight, implying that mice tolerate PB-Dpeg (or PB-Dpeg@nGO) NAs well without notable systemic toxicities. Whereas, 20% and 40% of the PBS- and free D-treated mice died during the monitoring period (Fig. S8D), respectively, and other treatment groups did not cause any notable intolerances, representing their better biocompatibilities compared with free D. Hematoxylin and eosin (H&E) staining further supported

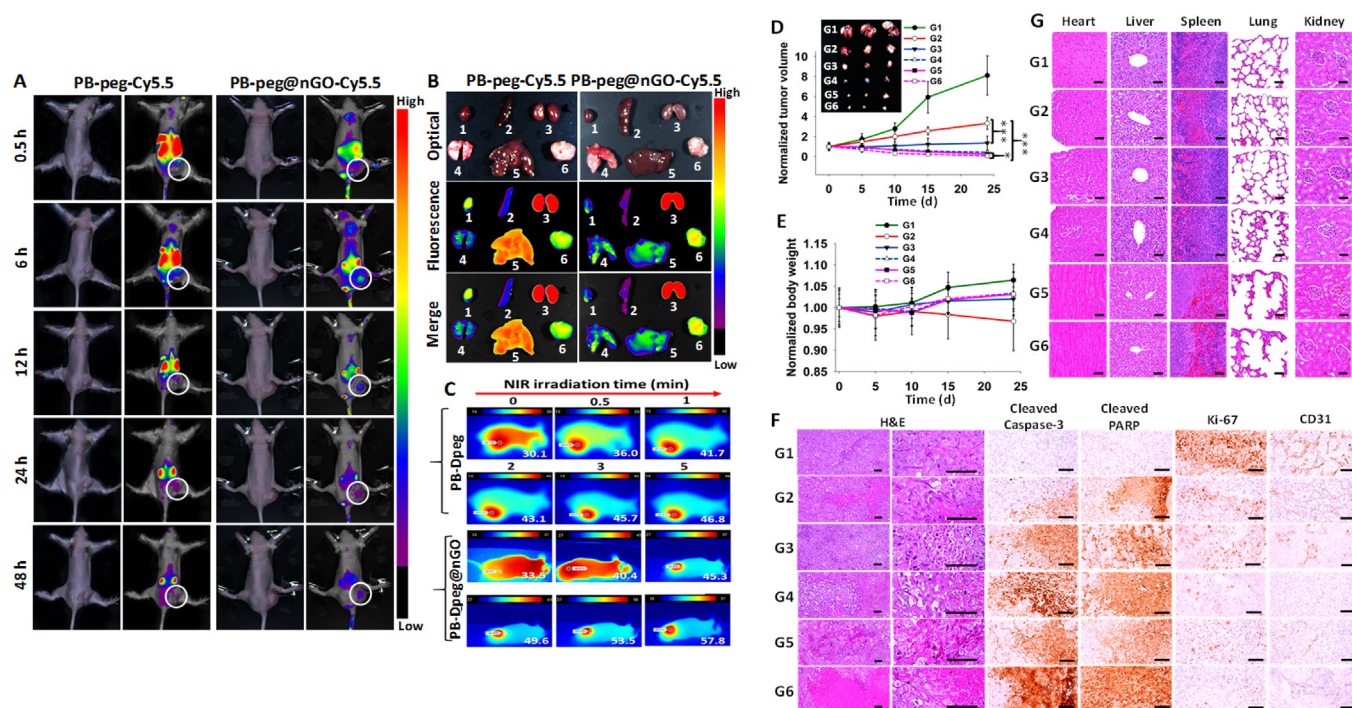


**Fig. 5.** *In vivo* (PANC-1 xenograft model) antitumor studies of NAs. (A, B) Whole-body (circles represent tumor regions) and ex vivo fluorescence distributions of Cy5.5-labeled NAs D-excluded forms to avoid fluorescence interference in major organs and tumors. 1: heart, 2: spleen, 3: kidney, 4: lung, 5: liver, and 6: tumor. (C) Time-dependent (0–5 min) temperature elevations of the treated (PB-Dpeg or PB-Dpeg@nGO) mice under NIR irradiation onto tumor regions. (D, E) Monitored tumor volume and body weight of treated mice (G1–G6). The treatment groups, G1, G2, G3, G4, G5, and G6, represent the untreated control, D, PB-Dpeg, PB-Dpeg (NIR), PB-Dpeg@nGO, and PB-Dpeg@nGO (NIR), respectively. Four injections were administered to mice ( $10 \text{ mg kg}^{-1}$ ) at 0, 3, 7, and 10 days (\* $p < 0.05$ , \*\* $p < 0.01$ , and \*\*\* $p < 0.001$ ). Inset digital image in (D) exhibits the tumors collected from the treated mice. H&E and immunocytochemically stained (cleaved caspase-3, cleaved PARP, Ki-67, and CD31) tumor section images (F) and histopathological images of major organs (G) from the six treatments (scale bars:  $120 \mu\text{m}$ ).

the observation of no notable toxicities from the NAs. Using immunohistological analysis (Table S2), the apoptosis markers-cleaved caspase-3 and cleaved PARP-were clearly observed in the two NAs, and were further intensified in the presence of NIR irradiation. The intensities of the proliferation (Ki-67) and angiogenesis (CD-31) markers were reduced in the treatments involving the two NAs, and were reduced further in the presence of NIR irradiation, demonstrating the antitumor effects of the NAs against pancreatic tumor cells. No noticeable histopathological changes were observed in heart, liver, spleen, lung, or kidney of the NA treated groups (Table S3). A hemolytic study was also conducted to examine the biosafety of the nGO adherence on the PB-Dpeg NAs (Fig. S8E). No significant generation of hemolysis was observed, nor were differences between the PB-Dpeg@nGO NAs with 10 and  $20 \mu\text{g mL}^{-1}$  of D content, although individual D clearly induced hemolysis. These results imply that nGO adherence on PB-Dpeg suppressed rapid D release to reduce hemotoxicities, but did not significantly induce adverse effects in red blood cells, providing further evidence for the applicability of PB-Dpeg modification using nGO for enhancing combination cancer therapy based on the vibrating spray approach.

#### 4. Conclusions

The development of a sprayable solution using a vibrating nozzle device and consisting of a clinically-approvable light-stimulatable vehicle, an anticancer drug, and a stealth component, produced NAs which appear to be effective for combination cancer phototherapy. The only modifications required for assembling PB-Dpeg NAs was prolonging the time of the hydrothermal reaction for securing porous PB (PB NC) to adsorb D and peg molecules, while a solution containing D and peg was directly mixed with the PB dispersion for spraying without any further treatments. The all-in-one droplets (PB

NC + D + peg) from the vibrating spray were subsequently solidified through ambient drying to form particulate PB-Dpeg, and the particulates were dispersed in buffered saline for direct use in anticancer studies. The NC's porosity also facilitated the patch up of PB-Dpeg with nGO to form PB-Dpeg@nGO, probably because of capillary action during the preparation, without significant changes to the size and shape of the PB-Dpeg. The *in situ* engineering to the treatment of PB, D, and peg appears to be a promising approach to the treatment of cancer using chemo-phototherapeutics both *in vitro* and *in vivo*. Patching up PB-Dpeg with nGO strengthened photothermal responses, sustained D release, and stealth effects (blood circulation to facilitate increased accumulation of the compound in tumors). The strategy proposed in this study not only provided a realizable engineering approach to the *in situ* assembly of clinically-approvable NAs for combination cancer phototherapy but also identified a convenient, low impact modification of the NAs to maximize the efficacy of the therapy.

#### Declaration of Competing Interest

The authors declare that they have no known competing financial interests or personal relationships that could have appeared to influence the work reported in this paper.

#### Acknowledgements

This work was supported by the National Research Foundation of Korea Grant funded by the Korean Government (NRF-2018R1A2B3001246). This research was also supported by the NRF (2018R1A2A2A05021143) grant funded by the Korean Government and the Medical Research Center Program (2015R1A5A2009124) through the NRF funded by MSIP.



## Appendix A. Supplementary data

Supplementary data to this article can be found online at <https://doi.org/10.1016/j.cej.2019.123177>.

## References

- [1] J. Peng, Q. Yang, W. Li, L. Tan, Y. Xiao, L. Chen, Y. Hao, Z. Qian, Erythrocyte-membrane-coated Prussian blue/manganese dioxide nanoparticles as  $H_2O_2$ -responsive generators to enhance cancer chemotherapy/photothermal therapy, *ACS Appl. Mater. Interfaces* 9 (2017) 44410–44422.
- [2] M.S. Moorthy, G. Hoang, B. Subramanian, N.Q. Bui, M. Panchanathan, S. Mondal, V.P.T. Tuong, H. Kim, J. Oh, Prussian blue decorated mesoporous silica hybrid nanocarriers for photoacoustic imaging-guided synergistic chemo-photothermal combination therapy, *J. Mater. Chem. B* 6 (2018) 5220–5233.
- [3] Y. Jeong, Y.K. Jo, B.J. Kim, B. Yang, K.I. Joo, H.J. Cha, Sprayable adhesive nanotherapeutics: mussel-protein-based nanoparticles for highly efficient locoregional cancer therapy, *ACS Nano* 12 (2018) 8909–8919.
- [4] J. Shao, C. Ruan, H. Xie, Z. Li, H. Wang, P.K. Chu, X.-F. Yu, Black-phosphorus-incorporated hydrogel as a sprayable and biodegradable photothermal platform for postsurgical treatment of cancer, *Adv. Sci.* 5 (2018) 1700848.
- [5] P. Xue, R. Yang, L. Sun, Q. Li, L. Zhang, Z. Xu, Y. Kang, Indocyanine green-conjugated magnetic Prussian blue nanoparticles for synchronous photothermal/photodynamic tumor therapy, *Nano-Micro Lett.* 10 (2018) 74.
- [6] X. Jia, X. Cai, Y. Chen, S. Wang, H. Xu, K. Zhang, M. Ma, H. Wu, J. Shi, H. Chen, Perfluoropentane-encapsulated hollow mesoporous Prussian blue nanocubes for activated ultrasound imaging and photothermal therapy of cancer, *ACS Appl. Mater. Interfaces* 7 (2015) 4579–4588.
- [7] L. Sun, Q. Li, M. Hou, Y. Gao, R. Yang, L. Zhang, Z. Xu, Y. Kang, P. Xue, Light-activatable chlorin e6 (Ce6)-imbedded erythrocyte membrane vesicles camouflaged Prussian blue nanoparticles for synergistic photothermal and photodynamic therapies of cancer, *Biomater. Sci.* 6 (2018) 2881–2895.
- [8] A. Sahu, J.H. Lee, H.G. Lee, Y.Y. Jeong, G. Tae, Prussian blue/serum albumin/indocyanine green as a multifunctional nanotheranostic agent for bimodal imaging guided laser mediated combinatorial phototherapy, *J. Control. Release* 236 (2016) 90–99.
- [9] T. Shang, J. Liu, Y. Chen, Z. Hu, L. Deng, H. Ran, P. Li, Y. Zheng, D. Wang, Z. Wang, Y. Sun, *In vivo* targeted cancer theranostics by core/shell-structured multifunctional Prussian blue/PLGA “nanococktails”, *Part. Part. Syst. Char.* 35 (2018) 1700306.
- [10] Z.L. Yang, W. Tian, Q. Wang, Y. Zhao, Y.L. Zhang, Y. Tian, Y.X. Tang, S.J. Wang, Y. Liu, Q.Q. Ni, G.M. Lu, Z.G. Teng, L.J. Zhang, Oxygen-evolving mesoporous organosilica coated Prussian blue nanoplateform for highly efficient photodynamic therapy of tumors, *Adv. Sci.* 5 (2018) 1700847.
- [11] C.R. Patra, Prussian blue nanoparticles and their analogues for application to cancer theranostics, *Nanomedicine (Lond.)* 11 (2016) 569–572.
- [12] D. Wang, J. Zhou, R. Chen, R. Shi, G. Zhao, G. Xia, R. Li, Z. Liu, J. Tian, H. Wang, Z. Guo, H. Wang, Q. Chen, Controllable synthesis of dual-MOFs nanostructures for pH-responsive artemisinin delivery, magnetic resonance and optical dual-model imaging-guided chemo/photothermal combination cancer therapy, *Biomaterials* 100 (2016) 27–40.
- [13] Y. Liu, G. Shu, X. Li, H. Chen, B. Zhang, H. Pan, T. Li, X. Gong, H. Wang, X. Wu, Y. Dou, J. Chang, Human HSP70 promoter-based Prussian blue nanotheranostics for thermo-controlled gene therapy and synergistic photothermal ablation, *Adv. Funct. Mater.* 28 (2018) 1802026.
- [14] X. Peng, R. Wang, T. Wang, W. Yang, H. Wang, W. Gu, L. Ye, Carbon dots/Prussian blue satellite/core nanocomposites for optical imaging and photothermal therapy, *ACS Appl. Mater. Interfaces* 10 (2018) 1084–1092.
- [15] G. Fu, W. Liu, S. Feng, X. Yue, Prussian blue nanoparticles operate as a new generation of photothermal ablation agents for cancer therapy, *Chem. Commun.* 48 (2012) 11567–11569.
- [16] P. Xue, J. Bao, L. Zhang, Z. Xu, C. Xu, Y. Zhang, Y. Kang, Functional magnetic Prussian blue nanoparticles for enhanced gene transfection and photothermal ablation of tumor cells, *J. Mater. Chem. B* 4 (2016) 4717–4725.
- [17] J. Cano-Mejia, R.A. Burga, E.E. Sweeney, J.P. Fisher, C.M. Bollard, A.D. Sandler, C.R.Y. Cruz, R. Fernandes, Prussian blue nanoparticle-based photothermal therapy combined with checkpoint inhibition for photothermal immunotherapy of neuroblastoma, *Nanomedicine* 13 (2017) 771–781.
- [18] W. Zhu, K. Liu, X. Sun, X. Wang, Y. Li, L. Cheng, Z. Liu,  $Mn^{2+}$ -doped Prussian blue nanocubes for bimodal imaging and photothermal therapy with enhanced performance, *ACS Appl. Mater. Interfaces* 7 (2015) 11575–11582.
- [19] W. Tian, Y. Su, Y. Tian, S. Wang, X. Su, Y. Liu, Y. Zhang, Y. Tang, Q. Ni, W. Liu, M. Dang, C. Wang, G. Zhang, Z. Teng, G. Lu, Periodic mesoporous organosilica coated Prussian blue for MR/PA dual-modal imaging-guided photothermal-chemotherapy of triple negative breast cancer, *Adv. Sci.* 4 (2017) 1600356.
- [20] Y.Y. Su, Z. Teng, H. Yao, S.J. Wang, Y. Tian, Y.L. Zhang, W.F. Liu, W. Tian, L.J. Zheng, N. Lu, Q.Q. Ni, X.D. Su, Y.X. Tang, J. Sun, Y. Liu, J. Wu, G.F. Yang, G.M. Lu, L.J. Zhang, A multifunctional PB@mSiO<sub>2</sub>-PEG/DOX nanoplateform for combined photothermal-chemotherapy of tumor, *ACS Appl. Mater. Interfaces* 8 (2016) 17038–17046.
- [21] B. Zhou, B.-P. Jiang, W. Sun, F.-M. Wei, Y. He, H. Liang, X.-C. Shen, Water-dispersible Prussian blue hyaluronic acid nanocubes with near-infrared photoinduced singlet oxygen production and photothermal activities for cancer theranostics, *ACS Appl. Mater. Interfaces* 10 (2018) 18036–18049.
- [22] W.-P. Li, C.-H. Su, L.-C. Tsao, C.-T. Chang, Y.-P. Hsu, C.-S. Yeh, Controllable CO release following near-infrared light-induced cleavage of iron carbonyl derivatized Prussian blue nanoparticles for CO-assisted synergistic treatment, *ACS Nano* 10 (2016) 11027–11036.
- [23] L. Jing, S. Shao, Y. Wang, Y. Yang, X. Yue, Z. Dai, Hyaluronic acid modified hollow Prussian blue nanoparticles loading 10-hydroxycamptothecin for targeting thermochemotherapy of cancer, *Theranostics* 6 (2016) 40–53.
- [24] H. Chen, Y. Ma, X. Wang, Z. Zha, Multifunctional phase-change hollow mesoporous Prussian blue nanoparticles as a NIR light responsive drug co-delivery system to overcome cancer therapeutic resistance, *J. Mater. Chem. B* 5 (2017) 7051–7058.
- [25] Z. Li, Y. Hu, T. Jiang, K.A. Howard, Y. Li, X. Fan, Y. Sun, F. Besenbacher, M. Yu, Human-serum-albumin-coated Prussian blue nanoparticles as pH-thermotriggered drug-delivery vehicles for cancer thermochemotherapy, *Part. Part. Syst. Char.* 33 (2016) 53–62.
- [26] Y.Y. Su, H. Yao, S. Zhao, W. Tian, W.F. Liu, S.J. Wang, Y. Liu, Y. Tian, X.D. Zhang, Z.G. Teng, G.M. Lu, L.J. Zhang, Ag-HPBs by a coating-etching strategy and their derived injectable implants for enhanced tumor photothermal treatment, *J. Colloid Interface Sci.* 512 (2018) 439–445.
- [27] L. Cheng, H. Gong, W. Zhu, J. Liu, X. Wang, G. Liu, Z. Liu, PEGylated Prussian blue nanocubes as a theranostic agent for simultaneous cancer imaging and photothermal therapy, *Biomaterials* 35 (2014) 9844–9852.
- [28] J. Li, F. Zhang, Z. Hu, W. Song, G. Li, G. Liang, J. Zhou, K. Li, Y. Cao, Z. Luo, K. Cai, “Pent-up” in hollow magnetic Prussian blue nanoparticles for NIR-induced chemo-photothermal tumor therapy with trimodal imaging, *Adv. Healthc. Mater.* 6 (2017) 1700005.
- [29] Z. Qin, Y. Li, N. Gu, Progress in applications of Prussian blue nanoparticles in biomedicine, *Adv. Healthc. Mater.* 7 (2018) 1800347.
- [30] J. Long, Y. Guari, C. Guérin, J. Larionova, Prussian blue type nanoparticles for biomedical applications, *Dalton Trans.* 45 (2016) 17581–17587.
- [31] W. Chen, K. Zeng, H. Liu, J. Ouyang, L. Wang, Y. Liu, H. Wang, L. Deng, Y.-N. Liu, Cell membrane camouflaged hollow Prussian blue nanoparticles for synergistic photothermal-/chemotherapy of cancer, *Adv. Funct. Mater.* 27 (2017) 1605795.
- [32] Q. Chen, C. Wang, X. Zhang, G. Chen, Q. Hu, H. Li, J. Wang, D. Wen, Y. Zhang, Y. Lu, G. Yang, C. Jiang, J. Wang, G. Dotti, Z. Gu, *In situ* sprayed bioresponsive immunotherapeutic gel for post-surgical cancer treatment, *Nat. Nanotechnol.* 14 (2019) 89–97.
- [33] S.W. Morton, K.P. Herlihy, K.E. Shopsowitz, Z.J. Deng, K.S. Chu, C.J. Bowerman, J.M. DeSimone, P.T. Hammond, Scalable manufacture of built-to-order nanomedicine: spray-assisted layer-by-layer functionalization of PRINT nanoparticles, *Adv. Mater.* 25 (2013) 4707–4713.
- [34] R. Altobelli, V. Guarino, L. Ambrosio, Micro- and nanocarriers by electro-fluidodynamic technologies for cell and molecular therapies, *Process Biochem.* 51 (2016) 2143–2154.
- [35] A.T. Barrows, A.J. Pearson, C.K. Kwak, A.D.F. Dunbar, A.R. Buckley, D.G. Lidzey, Efficient planar heterojunction mixed-halide perovskite solar cells deposited via spray-deposition, *Energy Environ. Sci.* 7 (2014) 2944–2950.
- [36] M. Bai, K. Xie, K. Yuan, K. Zhang, N. Li, C. Shen, Y. Lai, R. Vajtai, P. Ajayan, B. Wei, Scalable approach to dendrite-free lithium anodes via spontaneous reduction of spray-coated graphene oxide layers, *Adv. Mater.* 30 (2018) 1801213.
- [37] H. Li, Q. Yao, F. Xu, N. Xu, W. Sun, S. Long, J. Du, J. Fan, J. Wang, X. Peng, Lighting-up tumor for assisting resection via spraying NIR fluorescent probe of  $\gamma$ -glutamyltranspeptidase, *Front. Chem.* 6 (2018) 485.
- [38] M.A. Abdelmoneem, M. Mahmoud, A. Zaky, M.W. Helmy, M. Sallam, J.-Y. Fang, K.A. Elkhodairy, A.O. Elzoghby, Dual-targeted casein micelles as green nanomedicine for synergistic phytotherapy of hepatocellular carcinoma, *J. Control. Release* 287 (2018) 78–93.
- [39] P. Xue, L. Sun, Q. Li, L. Zhang, Z. Xu, C.M. Li, C.Y. Kang, PEGylated magnetic Prussian blue nanoparticles as a multifunctional therapeutic agent for combined targeted photothermal ablation and pH-triggered chemotherapy of tumour cells, *J. Colloid Interface Sci.* 509 (2018) 384–394.
- [40] M. Ming, N.L.K. Torad, Y.-D. Chiang, K.C.W. Wu, Y. Yamauchi, Size- and shape-controlled synthesis of Prussian blue nanoparticles by a polyvinylpyrrolidone-assisted crystallization process, *CrystEngComm* 14 (2012) 3387–3396.
- [41] R.K. Thapa, J.H. Byeon, S.K. Ku, C.S. Yong, J.O. Kim, Easy on-demand self-assembly of lateral nanodimensional hybrid graphene oxide flakes for near-infrared-induced chemothermal therapy, *NPG Asia Mater.* 9 (2017) e416.
- [42] G. Reina, J.M. González-Domínguez, A. Criado, E. Vázquez, A. Bianco, M. Prato, Promises, facts and challenges for graphene in biomedical applications, *Chem. Soc. Rev.* 46 (2017) 4400–4415.
- [43] L. Ou, B. Song, H. Liang, J. Liu, X. Feng, B. Deng, T. Sun, L. Shao, Toxicity of graphene-family nanoparticles: a general review of the origins and mechanisms, *Part. Fibre Toxicol.* 13 (2016) 57.
- [44] A.B. Seabra, A.J. Paula, R. de Lima, O.L. Alves, N. Durán, Nanotoxicity of graphene and graphene oxide, *Chem. Res. Toxicol.* 27 (2014) 159–168.
- [45] N. Zhu, S. Han, S. Gan, J. Ulstrup, Q. Chi, Graphene paper doped with chemically compatible Prussian blue nanoparticles as nanohybrid electrocatalyst, *Adv. Funct. Mater.* 23 (2013) 5297–5306.
- [46] E.E. Sweeney, J. Cano-Mejia, R. Fernandes, Photothermal therapy generates a thermal window of immunogenic cell death in neuroblastoma, *Small* 14 (2018) 1800678.
- [47] M. Gautam, S.K. Ku, J.O. Kim, J.H. Byeon, A scalable on-demand platform to assemble base nanocarriers for combination cancer therapy, *Nanoscale* 10 (2018) 11737–11744.
- [48] R.-Q. Song, H. Cölfen, Mesocrystals-ordered nanoparticle superstructures, *Adv. Mater.* 22 (2010) 1301–1330.
- [49] H. Maooui, R. Jijie, G.-H. Pan, D. Drider, D. Caly, J. Bouckaert, N. Dumitrascu, R. Chetoui, S. Szunerits, R. Boukherroub, 980 nm driven photothermal ablation of

- virulent and antibiotic resistant Gram-positive and Gram-negative bacteria strains using Prussian blue nanoparticles, *J. Colloid Interface Sci.* 480 (2016) 63–68.
- [50] S. Feng, H. Zhang, C. Zhi, X.-D. Gao, H. Nakanishi, pH-responsive charge-reversal polymer-functionalized boron nitride nanospheres for intracellular doxorubicin delivery, *Int. J. Nanomed.* 13 (2018) 641–652.
- [51] S. Zheng, X. Li, Y. Zhang, Q. Xie, Y.-S. Wong, W. Zheng, T. Chen, PEG-nanolized ultrasmall selenium nanoparticles overcome drug resistance in hepatocellular carcinoma HepG2 cells through induction of mitochondria dysfunction, *Int. J. Nanomed.* 7 (2012) 3939–3949.
- [52] M. Khalid, A.M.B. Honorato, Bendable tube-shaped supercapacitor based on reduced graphene oxide and Prussian blue coated carbon fiber yarns for energy storage, *J. Energy Chem.* 27 (2018) 866–873.
- [53] R. Krishna, E. Titus, O. Okhay, J.C. Gil, J. Ventura, E.V. Ramana, J.J.A. Gracio, Rapid electrochemical synthesis of hydrogenated graphene oxide using Ni nanoparticles, *Int. J. Electrochem. Sci.* 9 (2014) 4054–4069.
- [54] T. Jayaramudu, G.M. Raghavendra, K. Varaprasad, G.V.S. Reddy, A.B. Reddy, K. Sudhakar, E.R. Sadiku, Preparation and characterization of poly(ethylene glycol) stabilized nano silver particles by a mechanochemical assisted ball mill process, *J. Appl. Polym. Sci.* 133 (2016) 43027.
- [55] M. Wu, Q. Wang, X. Liu, J. Liu, Highly efficient loading of doxorubicin in Prussian blue nanocages for combined photothermal/chemotherapy against hepatocellular carcinoma, *RSC Adv.* 5 (2015) 30970–30980.
- [56] H. Ma, Y. Liu, M. Shi, X. Shao, W. Zhong, W. Liao W, M.M.Q. Xing, Theranostic, pH-responsive, doxorubicin-loaded nanoparticles inducing active targeting and apoptosis for advanced gastric cancer, *Biomacromolecules* 16 (2015) 4022–4031.
- [57] X. Li, Z. Qu, S. Jing, X. Li, C. Zhao, S. Man, Y. Wang, W. Gao, Dioscin-6'-O-acetate inhibits lung cancer cell proliferation via inducing cell cycle arrest and caspase-dependent apoptosis, *Phytomedicine* 53 (2019) 124–133.